Trailing Edge Flaps for Active Rotor Control
Aeroelastic Characteristics of the ADASYS Rotor System

Oliver Dieterich Bernhard Enenkl Dieter Roth
Oliver.dieterich@eurocopter.com Bernhard.enenkl@eurocopter.com Dieter.roth@eurocopter.com
Dynamics Engineers
EUROCOPTER Deutschland GmbH (ECD), Ottobrunn, Germany

Abstract
In the year 2005, a BK117 incorporating the ADASYS rotor system – the acronym is related to the German research project 'Adaptive Dynamische Systeme' (adaptive dynamic systems) – took off for the first flight. The four-bladed ADASYS rotor system is equipped with piezo-driven trailing edge flap units for active rotor control. In the meantime, the BK117 flew successfully with the flaps both in passive and active mode. Besides functionality tests, the already performed flights comprise a BVI noise reduction campaign and first tests for the adaptation of the vibration reduction controller. This paper gives an overview of the theoretical investigations and the related tests of the ADASYS rotor system. Emphasis is given on the aeroelastic characteristics and on the comparison with experimental results aiming towards the application of closed loop control of the active trailing edge flaps in flight for vibration reduction.

Notation

ADASYS	Adaptive dynamic systems
a_0, a_1	Coefficients
BVI	Blade Vortex Interaction
c_{fM}	Trailing edge flap hinge moment coefficient
c_D	Drag coefficient
c_L	Lift coefficient
c_M	Moment coefficient
CRC	Corporate Research Centre
DLR	Deutsches Zentrum fuer Luft- und Raumfahrttechnik
EADS	European Aeronautic Defence and Space Company
ECD	EUROCOPTER Deutschland GmbH
FW	Free wake analysis
Fxy	Hub in-plane force - N
Fz	Vertical hub force - N
IBC	Individual Blade Control
HHC	Higher Harmonic Control
LTI	Linear time invariant system
M	Mach number
Mxy	Hub out-of-plane moment - Nm
ONERA	Office National d'Etudes et de Recherches Aerospatiales
PW	Prescribed wake analysis
rev	Revolution
TEF	Trailing edge flap
TWG	Transsonic Windtunnel Goettingen
UI	Uniform Inflow
α	Angle of attack - deg
κ	Empirical factor
η	Flap deflection angle - deg
λ	Trailing edge flap chord ratio
$(\partial c_L/\partial\eta)/(c_{fM}/\partial\eta)$	Flap lift efficiency
$(\partial c_M/\partial\eta)/(c_{fM}/\partial\eta)$	Moment lift efficiency

Presented at the American Helicopter Society 62nd Annual Forum, Phoenix, AZ, May 9-11, 2006.

Introduction

Helicopter designers are fascinated from the technical possibilities offered by a high frequency and independent blade pitch control of main rotor blades. Main advantages are seen in the higher harmonic control of the lift distribution over the rotor plane directly affecting vibratory rotor loads, blade vortex interactions, stall delay and rotor performance. Side effects are identified in rotor control loads and rotor stability. Although during the last decades several organisations performed higher harmonic control studies confirming the high potential of such systems – especially in the fields of vibration and BVI (blade vortex interaction) reduction, the break through in the application of HHC (higher harmonic control) or IBC (individual blade control) culminating in a serial production of active rotor systems is still awaited.

At ECD, comprehensive experience exists with respect to a BO105 equipped with blade root actuation for IBC purposes. The pitch links of this experimental system were replaced by hydraulic actuators of high bandwidth allowing an individual blade pitch input for each blade of approximately 1 deg amplitude. While open loop flight tests demonstrated the controllability of this system with respect to vibrations and BVI noise, successful closed loop flight tests proofed the adequate choice of control algorithms for an efficient reduction of vibratory loads and BVI noise. As the investigated controllers for both vibration and noise control are of generic type and thus not restricted to an active rotor with blade root actuation, they can be applied to other actuation systems.

The change of the actuation system towards a piezo-actuated trailing edge flap for the active rotor – an actuation approach also investigated in detail in the United States [1, 2, 3] – was accompanied by a replacement of the test bed at ECD. An experimental BK117 helicopter serves now as prototype airframe. Compared to the BO105, both helicopters use a four bladed main rotor system with a hingeless rotor hub while the BK117 has an increased maximum take off weight. Regarding the aerodynamic design of the main rotor blades, the BO105 had conventional – serial production – rotor blades of rectangular planform and modified NACA airfoils while the blade geometry of the experimental ADASYS rotor system is identical to the EC145 showing advanced features e.g. ONERA airfoils and an optimised planform.

Although this geometrical similarity, the ADASYS rotor blades differ significantly from the serial production blades by aeroelastic and dynamic characteristics. The trailing edge flaps use a special modular design for maintenance purposes. The blades are built in such a way that the modules can easily be replaced thus requiring an open cross section in the trailing edge area of the blades. Therefore, stiffness and inertia characteristics differ significantly in the vicinity of the installation area of the trailing edge flaps. Furthermore, the blade tuning was modified for the special needs of this kind of active rotor system.

In contrary to the blade root actuation simply replacing the passive pitch link by an active actuator system, the implementation of trailing edge flaps offer the opportunity to tailor the design of the flaps with respect to the envisaged tasks. Design parameters of importance for the active flap are the radial position of the flap and the chord length of the flap. Lift and moment contributions generated by trailing edge flaps may work in parallel or counteract depending on the chosen flap design, the dynamic blade characteristics and the control task.

Regarding the full scale rotor system, whirl tower tests of the ADASYS rotor were performed in passive and active mode. Detailed comparisons between the experimental test results and the theoretical predictions took place. Special focus was given on the dependency of blade loads versus harmonic control input of the trailing edge flaps showing acceptable agreement. In the meantime, the flight test campaign of the BK117 incorporating the ADASYS rotor has started. First tests are dedicated to the check of rotor and overall system behaviour in passive mode and to the preparation of the open loop campaign with active trailing edge flaps.

The Forerunner: IBC Demonstrator BO105

The first IBC demonstrator operated by ECD was the BO105 S1 helicopter which was equipped by electro-hydraulic blade pitch actuators replacing the pitch links of the original control system in the rotating frame, see figure 1. For safety reasons the blade pitch authority of the actuators was limited by hardware stops to 1.1 deg. Although the authority was further reduced by software limits, the available IBC blade pitch amplitude proofed to be sufficient for impressive BVI noise reduction in descent flight [4] and for significant vibration reduction in level flight [5].

Figure 1: BO105 test bed for IBC by blade root actuation

The option of simultaneous control of vibration and noise was one of the key objectives in the controller architecture for the BO105 active rotor. Due to the four-bladed main rotor system, four input degrees of freedom are available represented by the four pitch link actuators of variable length. A transformation of these four input degrees of freedom into multi-blade coordinates allows the assignment of the collective, longitudinal and lateral IBC inputs to the vibration control task and the differential (or reactionless) IBC inputs to the BVI noise control task, see figure 2.

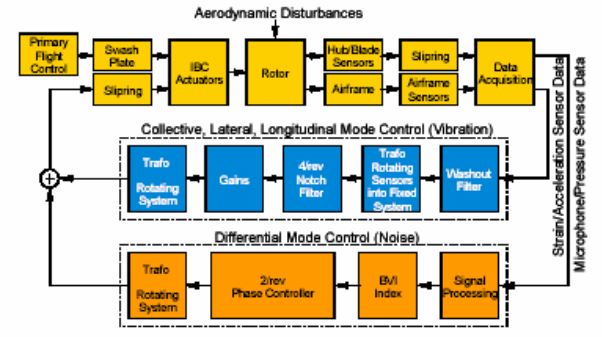

Figure 2: Controller architecture of combined vibration and BVI noise control

For BVI noise control, the usage of IBC is primarily related to the control of the miss-distance between blade tip vortices and rotor blade by variation of local lift distribution over the rotor disk. Typical BVI flight states e.g. descent flights generally show the property of blade tip vortices starting in front of the rotor disk with a significant upwash. Later – depending on the flight state i.e. flight speed and flight path – the tip vortices pass the rotor disk from top to bottom. Depending on the location where the tip vortices intersect the disk, BVI noise is generated in case a rotor blade is located in the vicinity of the tip vortex at the related rotor azimuth. If this event spans over a large ratio of the rotor blade at approximately the same time – a phenomenon designated as parallel BVI – a large noise level is emitted by the main rotor. For a four bladed rotor, the critical azimuth for parallel BVI on the advancing side is typically determined in the range between 30 deg and 60 deg.

Increasing the lift in a certain area of the rotor disk by additional blade pitch leads to augmented downwash lowering the trajectories of the tip vortices in this area. This effect allows the control of the locations of the rotor disk where the blade tip vortices pass the disk. Low frequency IBC inputs are especially efficient for manipulating the vortex paths as the vortex is affected over a long time leading to large miss-distances. As 1/rev inputs are related to flight control issues, 2/rev inputs are a natural choice for BVI noise reduction. Depending on the phase of 2/rev input, the locations where the tip vortices pass the rotor disk can be shifted towards the leading edge or the trailing edge of the rotor disk thus avoiding severe parallel BVI conditions. Regarding the amplitude of the 2/rev input, the selection of the maximum available amplitude showed generally the best benefit during flight tests with respect to noise reduction.

Regarding control theory and application, the plant behaviour is highly non-linear for BVI noise control. The high degree of non-linearity is reflected here by the control of a high frequency phenomenon – 20/rev and higher – by observing the pressure fluctuations on the rotor blade using a very low frequency input of 2/rev. Therefore, closed loop controllers are preferred which are not model-based as long as no simple models are available. The first BVI noise controller flown by the BO105 is based on an optimisation of the emitted sound using the Golden section rule. More advanced concepts using neural network techniques are under evaluation, see [6].

The development of the vibration reduction controller is initially aimed on the control of vibratory hub loads at blade passage frequency in the fixed system being the most dominant vibration source. The selected vibration controllers are based on disturbance rejection by output feedback. Due to the limit of three input degrees of freedoms in multi-blade coordinates, three hub load components were selected for disturbance rejection by output feedback applying linear control theory. For hingeless rotor systems like the BO105 or BK117 featuring a Boelkow rotor hub, the 4/rev hub roll and pitch moments are assessed to be of primary importance besides the 4/rev thrust components.

The disturbance rejection principle used by the vibration controller is based on the generation of vibratory counter-forces and moments of same magnitude and opposite sign cancelling out the vibratory hub load disturbance by superposition. In order to use this principle, the helicopter as plant is assumed to behave approximately linear in the sense that the superposition principle can be successfully applied. In this case the controller has to adjust the amplitude as well as the phase in order to achieve the cancelling condition. For this purpose the state space controller flown on the BO105 used dynamic compensators – notch filters tuned to the blade passage frequency – ensuring adequate robust control properties.

For appropriate stability characteristics of the closed loop system, the elements of a 6x3 gain matrix have to be adequately determined. A semi-empirical approach for the determination of the gain matrix was presented in [7]. This approach uses transfer functions describing the relationship between 4/rev inputs (collective, longitudinal and lateral blade pitch) and 4/rev outputs (thrust component, hub roll and pitch moments) in the

fixed system. Although the transfer functions were determined only for the 100 kts level flight case, the closed loop system proofed to be stable for level flights between 60 and 110 kts, for climbs and descents and for manoeuvre flight conditions, see [5].

Concluding the strategies of the different controller types, 2/rev blade pitch actuation is applied for noise control while 3/rev, 4/rev and 5/rev blade pitch actuation is used for vibration control in steady flight conditions. In this context, it should be highlighted that one of the reasons for the observed high level of controllability is seen in the relatively low fundamental torsion frequency of the BO105 main rotor blade below 4/rev. This low fundamental torsion frequency leads to an exaggeration of the effective blade pitch by superposing the elastic pitch generated by the torsion mode shape to the actuated blade pitch at the blade root, see figures 3 and 4.

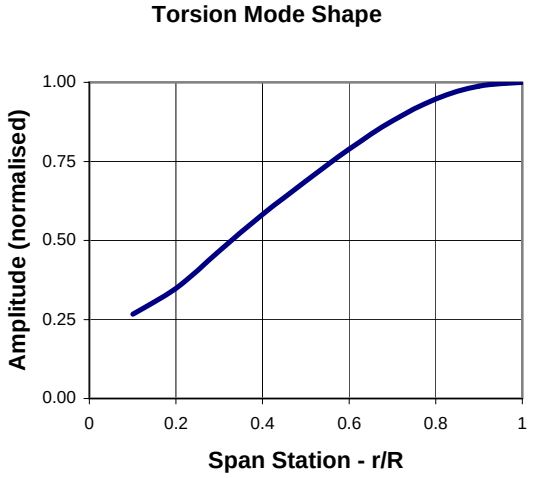

Figure 3: Calculated BO105 torsion mode shape

In the meantime, several components of the BO105 airframe as well as of the IBC system achieved their life time limits. Therefore, the BO105 was retired at the begin of 2005 with the advent of the BK117 equipped with the ADASYS rotor.

Background of the ADASYS Project

Although the electro-hydraulic actuators of the BO105 IBC proofed to behave well for the experimental campaign, a promising actuation concept for future applications was seen in piezo-actuated trailing edge flaps implemented in helicopter main rotor blades. One of the main reasons for this approach was the behaviour of the active elements and the main rotor system in case of failures. While the blade root actuators are integral parts of primary flight control therefore asking for high reliability, loss of functionality of the trailing edge flaps is assessed to be much less critical. Furthermore, the replacement of hydraulic power supply by electric power requires less mechanical complexity – e.g. avoidance of hydraulic sliprings – which is assumed to be beneficial for applications within smaller helicopters.

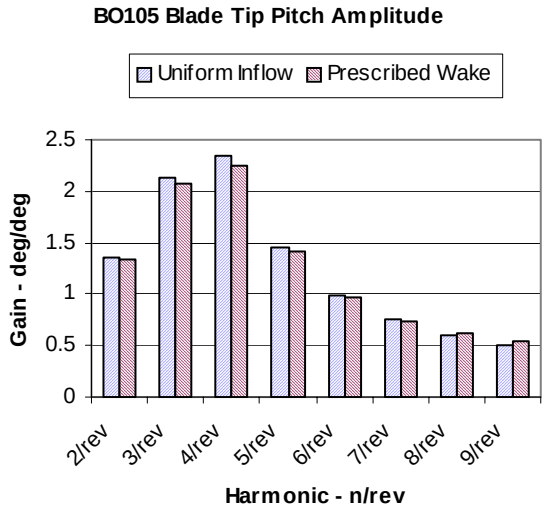

Figure 4: Calculated BO105 blade tip pitch response for different inflow models

Therefore, the ADASYS research project was twofold: The operation of the BO105 IBC was used for gaining basic knowledge in free flight conditions, for the evaluation of the potential offered by IBC for different disciplines and for testing of closed loop algorithms of different complexity for BVI noise and vibration reduction. On the other side, piezo-actuated trailing edge flap units were developed for the application on specially tailored helicopter main rotor blades in co-operation with EADS-CRC, see [8]. In order to provide appropriate benefit for various IBC applications, flap units and rotor blades have to be carefully tuned in order to fully exploit the potential of the active elements.

For the new test bed, a BK117 was selected to be equipped with the envisaged experimental rotor system. As shown in the following table, the BK117 is slightly larger than the BO105 being beneficial for space and weight requirements of the test equipment. Concerning the main rotor system, it should be noted that the rotor hub of type Boelkow is the same for both helicopters.

The design studies of the experimental rotor system started with the prototype blade of the EC145, see [9]. The planform of the blades has inboard tapering and features a swept back parabolic tip. The rotor spans over a diameter of 11 m and the equivalent chord amounts to 0.325 m. In [6], the non-dimensional fundamental blade torsion frequency is listed with 4.3/rev.

Compared to blade root actuation, the application of trailing edge flaps allows the careful selection of additional design parameters for the flaps. The following

three design parameters are of major importance for the efficiency of the trailing edge flaps:

- Trailing edge flap chord
- Trailing edge flap span
- Trailing edge flap location

Table 1: Comparison of IBC test beds operated by ECD

BO105 S1	BK117 S7045
Rotor radius 4.9 m	Rotor radius 5.5 m
Nominal TOW 2300 kg	Nominal TOW 3000 kg
Four bladed rotor with rotor hub type Boelkow	Four bladed rotor with rotor hub type Boelkow
Rectangular blade planform	Advanced blade planform
IBC by pitch link actuators generating displacements	IBC by trailing edge flaps generating lift and moment increments

In order to optimise these flap design parameters, corresponding aeroelastic rotor models were established and analysed by the CAMRAD II comprehensive rotorcraft code [10]. The implementation of trailing edge flaps into the rotor model required two steps: First, the extension of the airfoil tables in order to include the trailing edge flap angle and second the modification of stiffness and mass properties of the blades and the introduction of rigid bodies representing the trailing edge flaps by adequate inertia and being attached to the blade by two hinge locations.

Modification of Airfoil Tables

The aerodynamic layout of the rotor blade is based on airfoils of the last generations of the OA series from the French research organisation ONERA. For the table look-up approach of the applied rotor code, the aerodynamic coefficients (c_L, c_D, c_M) of the airfoils are compiled in table form depending on angle of attack and Mach number. For application of trailing edge flaps, these tables have to be extended by an additional dimension – the trailing edge flap angle – for those airfoil sections which are affected by the implementation of flaps. For the extension of the airfoil tables, only limited data based on wind tunnel tests of a trailing edge flap module and on CFD calculations [11, 12] existed at the time of application. Furthermore a high effort is seen in performing additional tests or additional calculations in order to gain the required table data for parameter investigations of the flap chord. Therefore, thin airfoil theory built the theoretical backbone in order to gather the required information concerning aerodynamic flap modelling as shown in appendix.

In order to demonstrate the proof of concept for a trailing edge flap driven by piezoelectric actuators, a blade section with embedded trailing edge flap was tested in the TWG wind tunnel Goettingen of DLR, see [11]. The blade section had a wing span of 1000 mm, a wing chord of 300 mm, a flap span of 500 mm and a flap chord of 45 mm leading to a flap chord ratio $\lambda = 0.15$. The wind tunnel test campaign focused on three different Mach numbers (nominal $M_\infty = 0.33$, 0.54, 0.74) representing the different flow speeds encountered by the trailing edge flap during a rotor revolution in forward flight.

In order to accompany the wind tunnel test campaign by theoretical studies, DLR performed numerical calculations based on two different procedures for the flapped airfoil undergoing arbitrary motions. On the one side, a theoretical approach combining Euler and boundary layer codes according to Drela-Zores was applied while on the other side numerical solutions based on the Navier-Stokes equations were analysed. These activities showed that the consideration of wall corrections affected significantly the measured results. Furthermore, the Euler/boundary layer and the Navier-Stokes codes demonstrated good agreement giving confidence to the numerical results. The results obtained by the Navier-Stokes code were finally selected for the calibration of the theoretical model of flap aerodynamics as outlined in appendix.

Implementation of the Trailing Edge Flaps

The definition of the trailing edge flap touches several physical aspects of the aeroelastic rotor modelling. Main points of interest are the influence of the trailing edge flap installation on inertia and stiffness characteristics in addition to aerodynamic issues of the rotor blades.

The applied rotor code offered the possibility to consider the trailing edge flaps as rigid bodies attached to the flexible rotor blade by two hinges. The locations of the hinges are defined by three coordinates in radial, chordwise and normal direction of the rotor blades. For the definition of the rigid body, flap mass, flap center of gravity and flap moment of inertia about the hinge axis are required data. An approximation for the inertia data given below for a TEF chord of 45 mm is based on the experience of DLR gained by the wind tunnel test program.

- Flap Mass 0.1 kg/m
- Flap Inertia Moment 0.0000169 kgm
- Chordwise C.G. 15 mm

In order to assign flexibility and damping to the flap actuator, the implementation of hinge spring and hinge damper providing stiffness and viscous damping are typical means in multibody codes. For the first step presented here, actuator dynamics are neglected within

the parameter investigations. Using a penalty approach, high spring stiffness is assigned in order to achieve a quasi-steady behaviour of the hinge joint degree of freedom. Consequently, the deflection of the trailing edge flap is controlled by prescribed values entered by the user.

The implementation of a trailing edge flap leads to a partial re-design of the rotor blade at least at the radial stations of the trailing edge flap. Special cut-offs have to be considered during design process in order to allow the installation of the actuation modules. These cut-offs have an impact on local stiffness and inertia data as well as on the locations and directions of the corresponding axes (elastic axes, tension center axes, center of gravity axes). For the parameter studies of the first phase, no modifications of this kind are considered for the rotor blade definition.

According to the actuation system design of the wind tunnel tests, the foreseen trailing edge flap is segmented into two pieces (figure 5); each piece deflected by two actuator units. For the modelling of the flap actuation, the trailing edge flap of the rotor model is divided into four pieces; one actuator unit being assigned per segment. Each actuator unit is considered as point mass centered on the quarter chord line in the middle of the flap piece. With respect to the baseline rotor, the actuator masses are the main modifications changing the structural dynamic behaviour of the rotor.

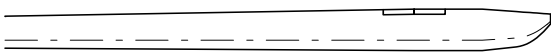

Figure 5: Blade featuring two flap pieces (chord 45 mm)

Due to the fact that linearized thin airfoil theory is used, the user has to observe restrictions for Mach numbers and angles of attack in the trailing edge flap section as well as for the flap deflection angle. For the implementation of the Mach number dependency, compressibility effects of the derivativa are considered according the Prandtl-Glauert rule up to a Mach number of 0.75. For higher Mach numbers, the compressibility corrections are limited to Mach number 0.75 in order to avoid numerical problems associated with the singularity at sonic speed for linearized aerodynamics. For the envisaged application of the trailing edge flap, operational conditions in the transonic regime have several disadvantages and will be consequently avoided by design. Therefore, the restriction of the flap aerodynamic data to the above mentioned limit poses no serious restriction.

The aerodynamic behaviour of a trailing edge flap at high angle of attacks is highly non-linear as stall effects are very sensitive to the flow pattern at the rear top region of the airfoil. Therefore, the assumptions for the linearized thin airfoil theory are limited to attached flow conditions. For the operation of the trailing edge flap under significant stall conditions, the flap airfoil data have to account for all the phenomena associated with stall. In the present approach, no corrections exist for the non-linear behaviour at higher angle of attack. This procedure is justified as long as the trailing edge flap sections are not affected by significant stall effects. Furthermore, reverse flow conditions are not appropriately taken into account as this special case is not implemented separately. Nevertheless, these restrictions do not have any major impact on the presented investigations, as the flap layout prefers a more outboard integration of the flap on the blade by theoretical reasons.

Furthermore, the linear relationship between flap deflection angle and flap induced lift and moment by thin airfoil derivativa is implemented for a selected interval of +/-20 deg for flap deflection. For larger flap angles, the lift and moment contributions of the flap are linearly decreased until reaching zero at +/-90° deflection angle simulating separated flow at the flap. This is only a very simple model in order to allow the completion of the airfoil tables for all numerically possible flap deflection angles. Of course, the real aerodynamic behaviour of the trailing edge flap is much more complicated and has to be measured or calculated by CFD, if necessary. In case of the presented application of a piezo-actuated trailing edge flap, the maximum deflections depend on the characteristics of the actuator and are within a range allowing the approximation of the aerodynamic coefficients by linear relations.

Parameter Investigations: “Hover” Case

In order to get a better understanding of rotors equipped with trailing edge flaps, the first step of the studies focused on axisymmetric environmental conditions. Hereby, the rotor is trimmed to a thrust of approximately 35 kN repesenting the actual maximum take-off weight of the EC145. Based on the experience of the BO105 the HHC input of 3/rev, 4/rev and 5/rev is assessed to be most effective for the reduction of hub load induced vibrations for a four-bladed rotor. Therefore, the performance of the trailing edge flap designs is investigated with respect to 3/rev, 4/rev and 5/rev control input. For these studies, a representative trailing edge flap deflection of 5 deg is applied corresponding to the capabilites of the envisaged piezo actuator systems. For the parametric studies, a uniform inflow model is applied for representation of the induced velocities of the rotor wake. Therefore, it should be kept in mind that uniform inflow slightly overpredicts the performance of the trailing edge flaps due to missing 3D effects at the end of the flaps.

The first step of the parameter investigations consisted in investigating the role of the radial location of the

trailing edge flaps. For these studies, the active span of the rotor blade amounts to 500 mm while the flap chord was selected to 45 mm leading to a flap chord ratio of approximately 15%. Due to the non-rectangular planform of the blade, the flap chord ratio slightly varies along span. Table 2 and figure 6 present the radial locations of the flap boundaries in span direction.

Table 2: Flap radial locations (Rotor radius 5.5 m)

Flap Config.	TEF inboard radius %	TEF middle radius %	TEF outboard radius %
1	85.5	90.0	94.5
2	80.0	84.5	89.1
3	75.5	80.0	84.5
4	70.9	75.5	80.0
5	66.4	70.9	75.5
6	61.8	66.4	70.9
7	57.3	61.8	66.4

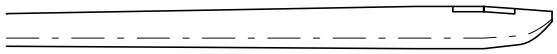

Flap configuration 1

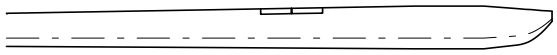

Flap configuration 7

Figure 6: Range of investigated trailing edge flap radial locations

The results of figure 7 are related to a trailing edge flap actuation of 4/rev. For this case the trailing edge flap operates at a frequency of 4/rev in the rotating system leading to simultaneous reaction and motion of all blades. With the exception of the torque moment, the only hub load component excited by this actuation mode is the vertical hub force. According to figure 7, the generated 4/rev vertical hub force component depends on the location of the trailing edge flap showing a maximum in the vicinity of 4.3 m. In order to explain this maximum, two effects have to be considered while varying the trailing edge flap in spanwise direction. First, four point masses representing the actuators are aligned to the flap in spanwise direction leading to a change in the dynamic tuning of the rotor blades. Second, the different arrangements of the trailing edge flap result in a different excitation of the blade modes with respect to TEF attachment in spanwise direction (oscillation nodes and antinodes) and load amplitude (varying chord and dynamic pressure).

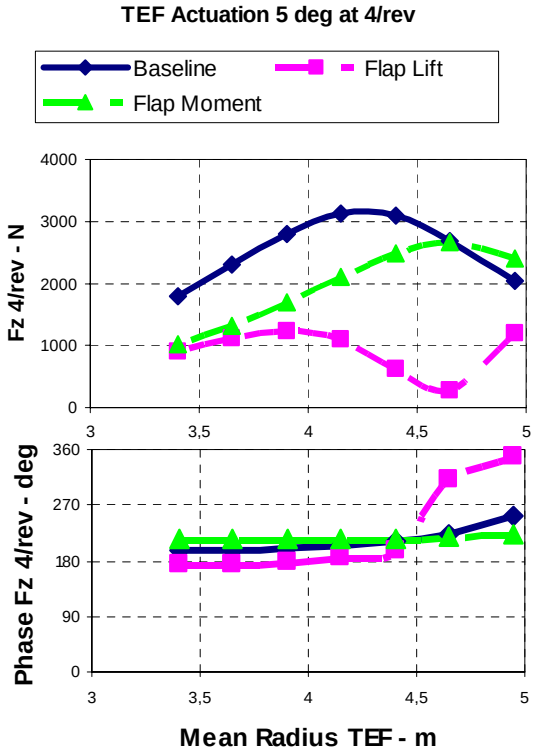

Figure 7: 4/rev vertical hub force response versus trailing edge flap location, "hover"

In order to separate these effects, the actuator masses are eliminated from the structural model in a second run. Thus, the spanwise location of the trailing edge flap does not alter the tuning of the rotor blades in this case. The general trends obtained by these calculations are very similar to those of the baseline case, only the amplitudes differ slightly. Therefore, it can be concluded that the excitation of the blade modes by aerodynamic loads at different locations dominates significantly compared to the altered tuning of the blades.

If the trailing edge flap is deflected, a change of lift and moments occurs within the region of the trailing edge flap. Regarding an elastic rotor blade, the pitch moment changes interact primarily with the torsion modes of the blade whereas the lift changes excite mainly the flap bending modes of the blade. In order to explain the location of the maximum amplitude, lift and pitch moment effects of the trailing edge flaps are separated by modification of the corresponding airfoil table. Airfoil tables are created only considering the trailing edge flaps affecting the lift coefficients or the moment coefficients. In the first case, the influence of the trailing edge flaps on aerodynamic pitch moments is totally suppressed. In figure 7, this case is designated as 'Flap Lift'. In the second case only aerodynamic moment coefficients are altered – thus eliminating any lift changes due to the deflected flap. The designation of this case used in the figures is 'Flap Moment'.

The results for the 'Flap Lift' and the 'Flap Moment' cases in figure 7 allow an insight in the mechanisms of hub load excitation by trailing edge flaps. Analysing the cosine and sine components of the different cases, an almost linear behaviour of the aerodynamic flap induced loads is noticed for the selected trailing edge flap actuation of 5 deg at 4/rev by summing up the cosine and sine contributions of the 'Flap lift' and 'Flap moment' cases and comparing with the baseline results. In this context, it should be mentioned that the rotor model is based on non-linear equations.

The amplitude of the 'Flap Moment' case shows an almost monotonic increase explainable by the increase of the dynamic pressure in combination with the fundamental torsion mode shape, see figure 8, while shifting the trailing edge flaps outboard. The decrease of the hub force amplitude at the most outboard position is probably related to the decreasing blade chord in this section.

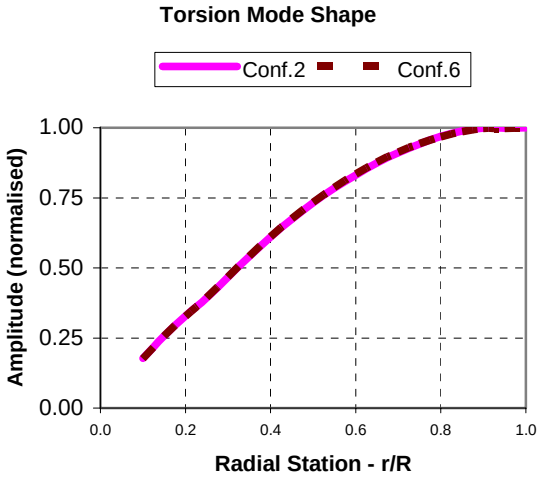

Figure 8: Torsion mode shape for different locations of the actuation inertia masses (conf.2: TEF center at 84.5%, conf.6: TEF center at 66.4%)

Phase angles are also plotted for the baseline case, the 'Flap Lift' case and the 'Flap Moment' case in figure 7. While the 'Flap Moment' case shows almost constant phase values – the excitation is given by a cosine function, a phase shift of approximately 180 deg is noted for the 'Flap Lift' case between 4.3 m and 4.6 m.

Concerning the 'Flap Lift' case, the location of the trailing edge flap with respect to the oscillating nodes and anti-nodes of the blade flapping modes is of major importance for the amplitude and phase of the hub loads. In the following figures 9 and 10, blade mode shapes are presented of the second and third blade flap modes which are especially excited by 4/rev actuation. The correlation between minimum gain and significant phase shift of the 4/rev hub load response at a radial position of approximately 4.6 m and the nodes of the second and third flap modes in the neighbourhood of this radial station is obvious. Passing the node by shifting the TEFs towards more outboard positions leads to a phase jump of 180 deg due to changed sign of the mode shape deflection.

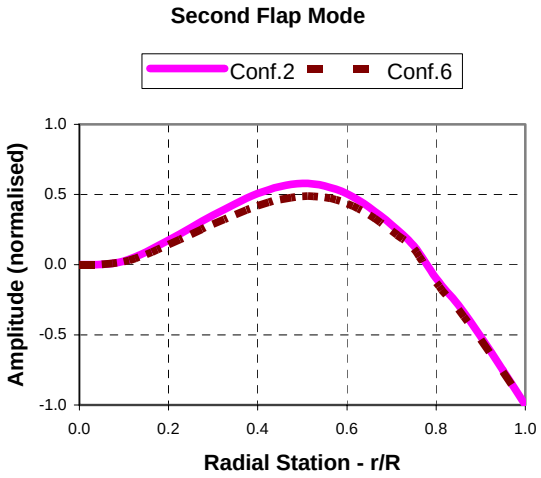

Figure 9: Second flap mode shape for different locations of the actuation inertia (conf.2: TEF center at 84.5%, conf.6: TEF center at 66.4%)

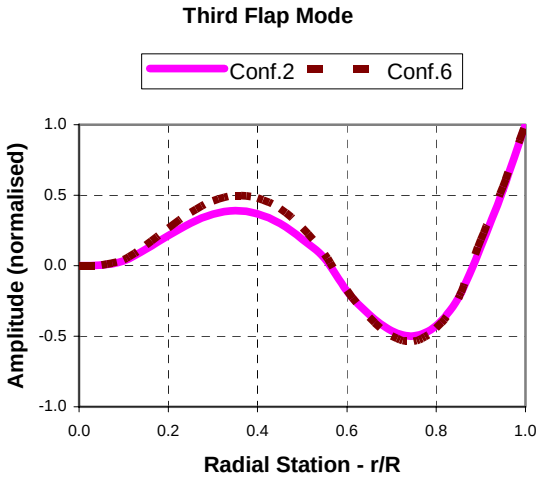

Figure 10: Third flap mode shape for different locations of the actuation inertia (conf.2: TEF center at 84.5%, conf.6: TEF center at 66.4%)

Corresponding results from flap lift and flap moments are obtained analysing the in-plane hub forces and the out-of-plane hub moments for 3/rev or 5/rev flap actuation. For the vibration reduction purpose, these loads are of special interest in the fixed airframe system. Due to the transformation from the rotating system to the non-rotating system, the 3/rev and 5/rev components of the in-plane forces and out-of-plane moments map to 4/rev longitudinal and lateral hub in-plane forces and

4/rev hub pitch and roll moments respectively. For these actuation frequencies, low hub load controllability is observed for the outboard flap locations due to counteracting contributions from lift and moment culminating in several minima at span station 4.6 m, see figures 11 and 12 for 3/rev input and figures 13 and 14 for 5/rev input. These results underline the need of a careful flap design in order to achieve the requirements for vibration reduction in an optimum way.

In figure 15, maximum and minimum flap hinge moments are plotted for 4/rev actuation. As expected the peaks of the flap hinge moments increase while shifting the flaps outboard due to increasing dynamic pressure thus augmenting aerodynamic flap loads. Investigating the flap loads only caused by inertia – labelled "Inertia Loads max" and "Inertia Loads min" – it is noted that the change of the flap loads is substantially smaller than in the baseline case where aerodynamic flap hinge moments are taken into account.

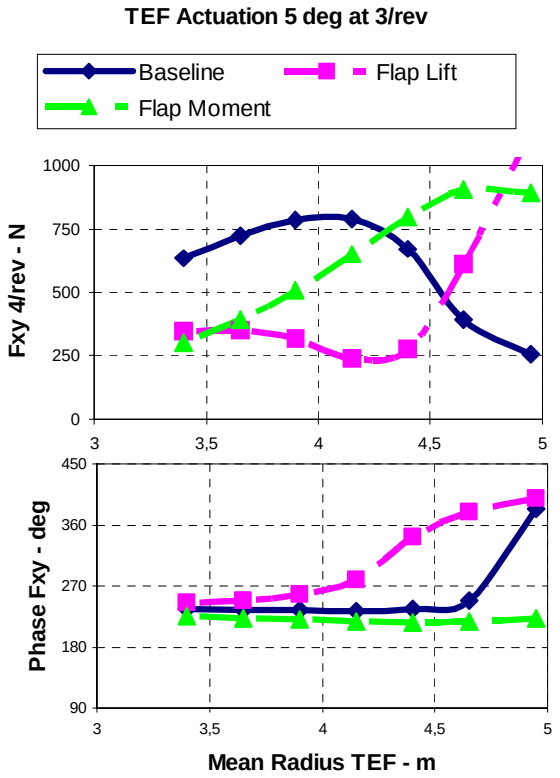

Figure 11: 4/rev in-plane hub force response versus trailing edge flap location for 3/rev input, "hover"

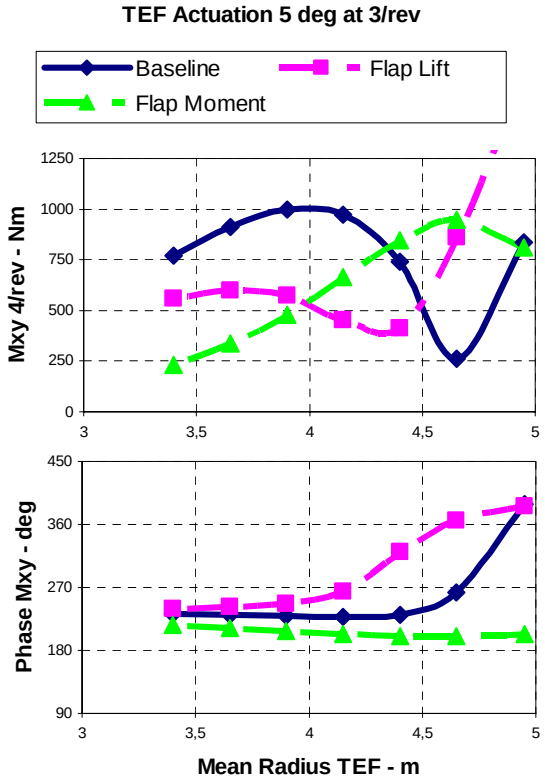

Figure 12: 4/rev hub out-of-plane moment response versus TEF location for 3/rev input, "hover"

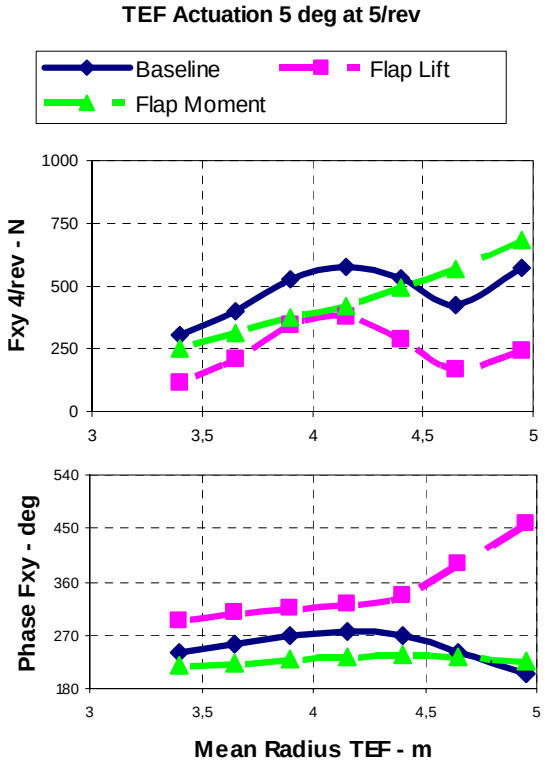

Figure 13: 4/rev in-plane hub force response versus trailing edge flap location for 5/rev input, "hover"

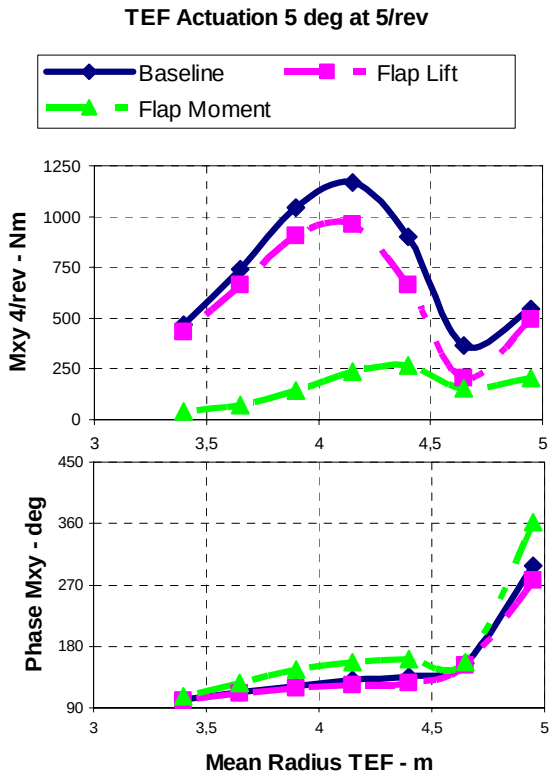

Figure 14: 4/rev hub out-of-plane response amplitude versus TEF location for 5/rev input, "hover"

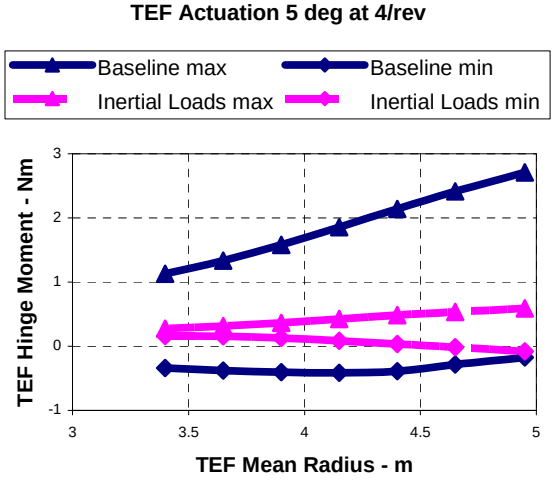

Figure 15: Trailing Edge Flap Hinge Moments

Parameter Investigations: Level Flight

In forward flight, the operating conditions of the trailing edge flap changes significantly compared to axial flow as the rotational velocity of the blade section is superposed by the forward flight speed. The dynamic pressure and the Mach number show significant rotor periodic variations affecting the aerodynamic loads generated by the trailing edge flap. Furthermore, 4/rev hub loads exist without actuated trailing edge flap, too. Therefore, the following plots show only the difference between actuated trailing edge flap case and fixed trailing edge flap case (reference case: no flap deflection). For the presented investigations, a forward flight state at 130 KTAS is selected as design point. In order to simulate the flight conditions the rotor is trimmed to thrust and hub moments measured by flight tests. Furthermore, the shaft axis of the rotor is oriented taking into account helicopter roll and pitch attitude.

Due to the asymmetry caused by the forward flight, the parameter investigations have to consider the actuation phase angle of the trailing edge too. For each actuation frequency, the phase of the trailing edge flap actuation ranges from 0 deg to 330 deg with a step size of 30 deg. A phase value of 0 deg is related to maximum trailing edge flap deflection downwards on the reference blade which points rearwards at zero rotor azimuth angle. Furthermore – due to the periodically varying flow conditions – every investigated actuation frequency (3/rev, 4/rev, 5/rev) affects all hub load components at blade passage frequency. Therefore, only selected results of the forward flight case are presented below focussing on the influence of trailing edge flap actuation on 4/rev vertical hub, see figures 16 to 18. As can be seen the best controllability of the vertical hub force is obtained for flap configuration 3 (radial location 80%). This result is in good agreement with the studies of the hover case presented above. Furthermore, it should be noted that this optimum of the trailing edge flap radial position is also obtained for the other hub load components.

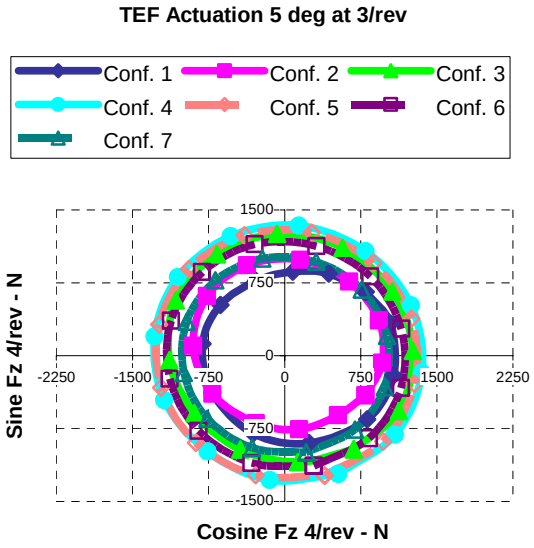

Figure 16: 4/rev hub vertical force vs TEF location in forward flight for 130 kts and 3/rev input

Based on these results, the next step focussed on the role of the trailing edge flap chord as design parameter. Trailing edge flaps are mainly used in order to alter aerodynamic lift or moment of the rotor blade. For the actuation of trailing edge flaps, a device is needed in

order to deflect the trailing edge flap. Typically, this device has to act against hinge moments thus requiring force and power generating capabilities which should be kept to a minimum by flap design. Full scale whirl tower tests featuring a variation of the flap chord ratios are reported in [13].

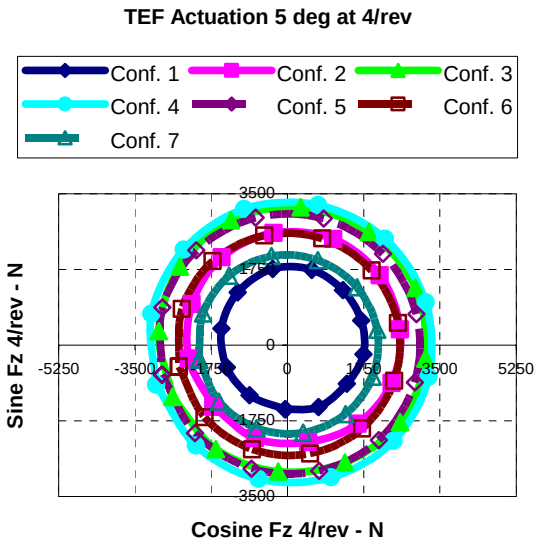

Figure 17: 4/rev hub vertical force vs TEF location in forward flight for 130 kts and 4/rev input

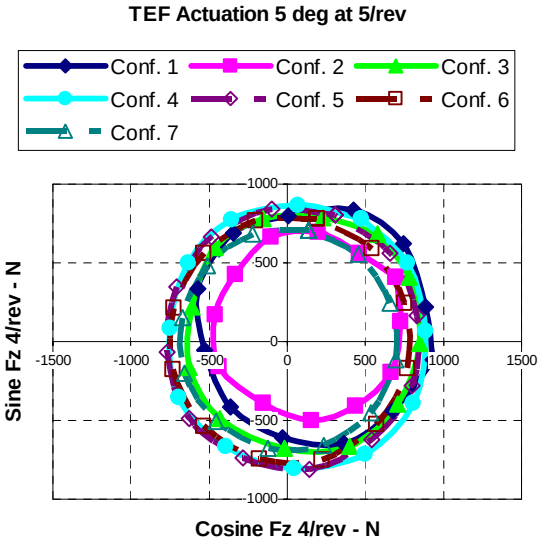

Figure 18: 4/rev hub vertical force vs TEF location in forward flight for 130 kts and 5/rev input

If the application of the flap is particularly aimed on lift control, the altered lift has to be related to the required hinge moments as target objective for efficiency studies. In order to visualize this approach, the ratio $(\partial c_L/\partial\eta)/(\partial c_{fM}/\partial\eta)$ – labelled as lift efficiency – is plotted versus flap chord ratio in figure 19. In this figure, the existence of two poles for λ approaching zero and λ approaching unity is noteworthy. Realistic flap chord ratios are assumed between 10% and 30%. Regarding this interval, the diagram shows that smaller flap chord ratios are more efficient with respect to flap hinge moments. This behaviour is in coincidence with general aerodynamic knowledge that the trailing edge conditions highly affects circulation and thus lift. Therefore, small changes in the trailing edge region lead to major reactions of the flowfield. The more the flap is located at the trailing edge flap, the more the flap is efficient with respect to actuation power.

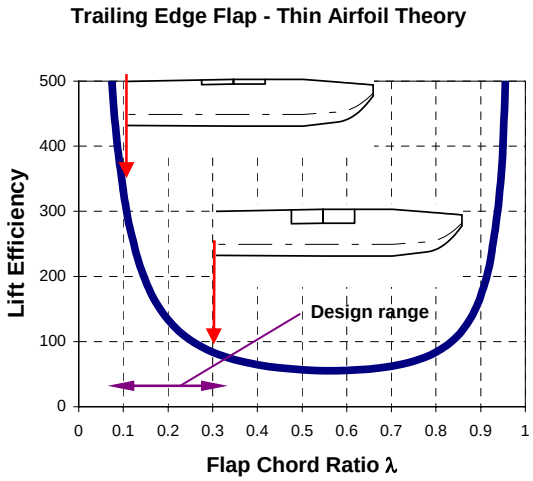

Figure 19: Flap lift efficiency versus trailing edge flap chord ratio

Concerning moment control e.g. servo flaps, this procedure is transferred to the comparison of moment changes with hinge moment changes. In figure 20, the ratio $(\partial c_M/\partial\eta)/(c_{fM}/\partial\eta)$ – labelled as moment efficiency – is used for the demonstration of flap efficiency. This figure shows also a pole for the flap chord ratio approaching zero which is a similar behaviour for small λ as observed in figure 19. Corresponding to the lift control case, the flap is again most efficient at small flap chord ratios.

These conclusions are also confirmed by parameter studies of the rotor model. Regarding the related numerical studies, the flap chord is not fixed to a constant chord length of 45 mm but to a constant flap chord ratio λ varying from 10% to 30% in 5% steps. The following figures 21 to 25 show the influence of the flap chord to the hub load controllability for the axialsymmetric test case. Interestingly, the main part of hub load controllability is already achieved by 10% flap chord ratio. The doubling of the flap chord ratio from 10% to 20% leads only to an increase by approximately one third. In case of 15% and 30% flap chord ratio, the hereby gained performance increment is even less.

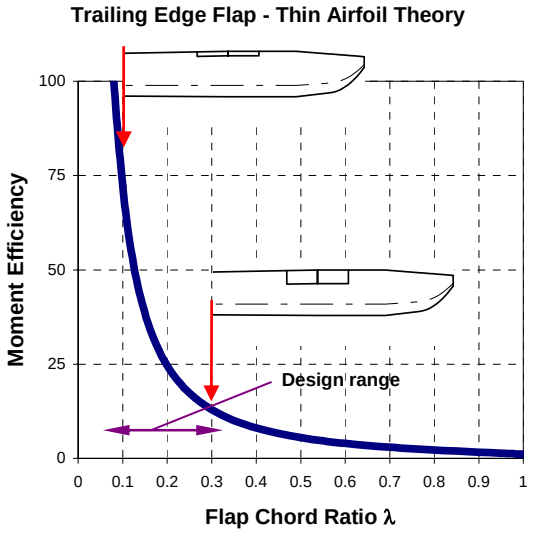

Figure 20: Flap moment efficiency versus trailing edge flap chord ratio

For practical applications a compromise has to be found between control efficiency – meaning small flap chord ratios – and control authority – meaning adequate flap size. If the deflection angles increases too much, a flow separation will occur at the trailing edge flap leading to performance losses and increased drag. In this case, an increase of the flap length is recommended. Furthermore, the minimum flap chord is typically defined by design constraints e.g. by minimum flap thickness limitations needed for integration as it is the case for the ADASYS rotor system.

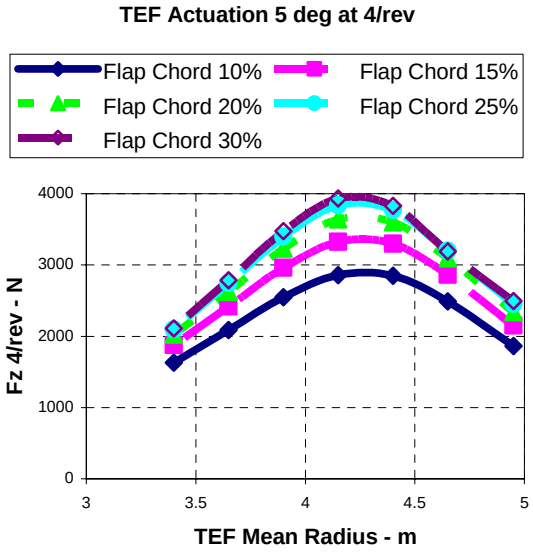

Figure 21: 4/rev vertical hub force for varying TEF chord ratios, 4/rev input, "hover"

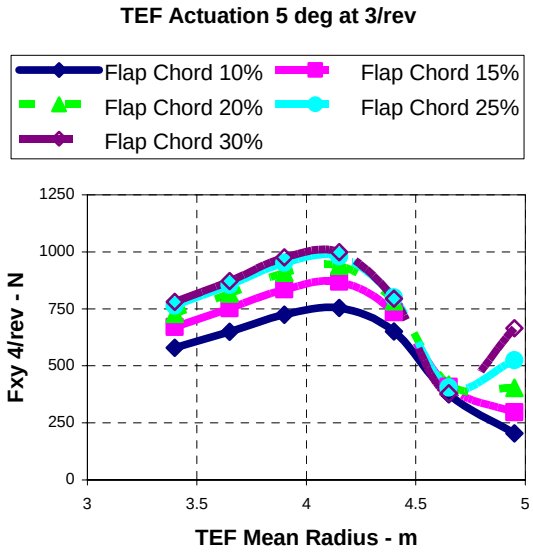

Figure 22: 4/rev in-plane hub force for varying TEF chord ratios, 3/rev input, "hover"

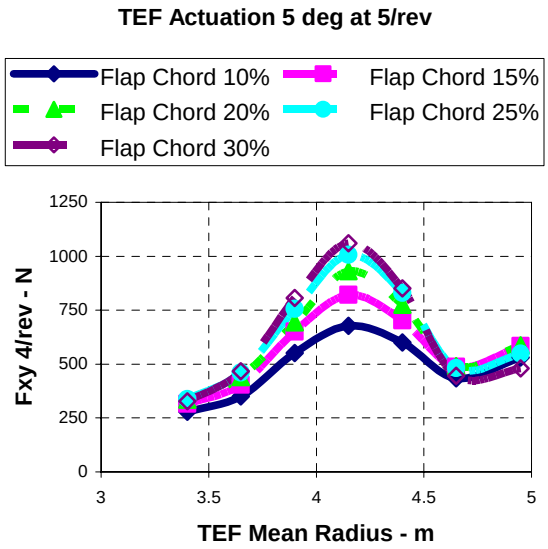

Figure 23: 4/rev in-plane hub force for varying TEF chord ratios, 5/rev input, "hover"

Realisation of the ADASYS Rotor

In accordance to the results of the parameter investigations, the final flap design is related to the smallest possible trailing edge flap chord of 0.05 m [8]. Furthermore, the span of each actuation unit was increased from 250 mm to 300 mm due to improvement of actuator performance. The ADASYS rotor can be equipped with up to three actuation units located at 3.95 m (71.8%), 4.25 m (77.3%) and 4.55 m (82.7%). The following table summarises the data of the active flap system based on two active modules at the inboard stations:

Table 3: Active flap system

Flap chord	0.05 m
Flap chord ratio (based on equivalent blade chord)	15.6%
Active flap span	0.6 m
Flap span ratio	10.9%
Active flap center	4.1 m
Flap center ratio	74.5%

Furthermore, the rotor blade dynamic characteristics were changed. Besides the modification of the cross-section design in the radial range of the flaps, tuning masses and the serial blade flap absorber were eliminated. In addition, the torsion frequency of the blade was lowered in order to achieve an optimum response of the trailing edge flaps when actuated in the vicinity of the blade torsion frequency.

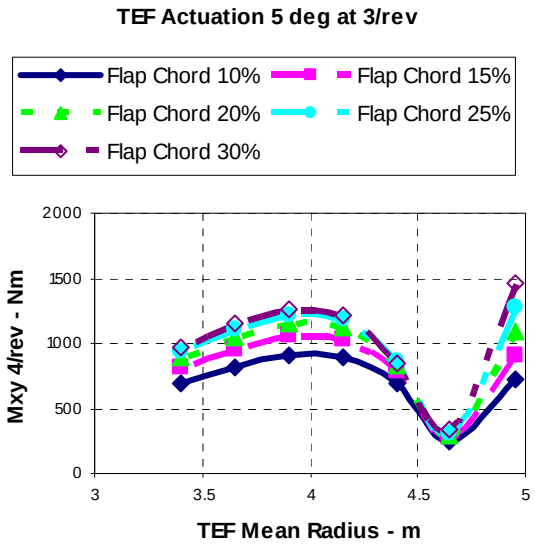

Figure 24: 4/rev hub out-of-plane moment for varying TEF chord ratios, 3/rev input, "hover"

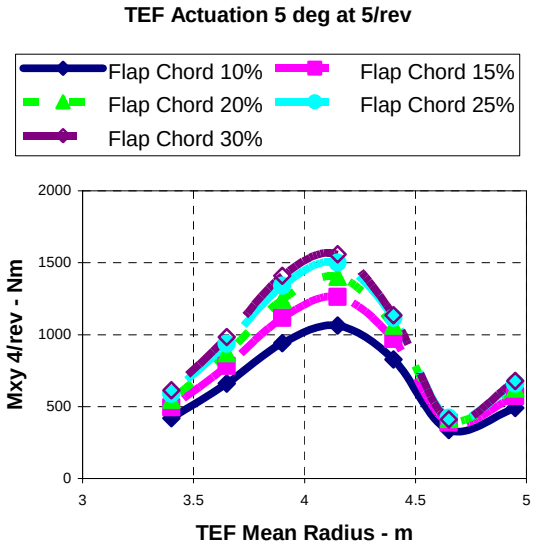

Figure 25: 4/rev hub out-of-plane moment for varying TEF chord ratios, 5/rev input, "hover"

Whirl Tower Testing

Two whirl tower test campaigns were performed in 2002 and 2004. Regarding the tests in 2002, only a two blade configuration was experimentally investigated with emphasis on basic functionality tests of the blades and the trailing edge flap units. Measurements were performed with respect to blade modal frequencies and blade characteristics regarding static and dynamic trailing edge flap actuation. During these tests, only one unit per blade incorporating an active trailing edge was applied while the other locations were provided with dummy modules. The 2004 test campaign using the fully equipped rotor was directly aimed on preparing the active rotor towards flightworthiness. This time, the rotor had two active trailing edge flaps per blade in the inboard positions while dummy modules were put at the outboard position, see figure 26. Rotor performance and blade loads were also objectives of the experimental campaign with all blades installed.

Figure 26: ADASYS rotor on whirl tower test stand (2004)

The whirl tower tests were complemented also by theoretical activities. Figure 27 shows the comparison of blade modal frequencies measured at the whirl tower with the results of the numerical rotor model. Due to available actuation performance, TEF hinge moments are of major interest. Figure 28 shows the predicted actuator loads for static deflections of the TEF while figure 29 presents the corresponding measured quantities. As a slight difference in the slope versus collective setting was noted, the influence of both TEF centre of gravity and aerodynamic loading was analysed in figures 30 and 31 demonstrating that the differing behaviour can be explained by related modelling uncertainties. The reader is remembered here to the approximations mentioned above with respect to the modelling the flap hinge moment coefficients. Figures 32 and 33 show an adequate agreement of the TEF hinge moments in the context of the actuation limits.

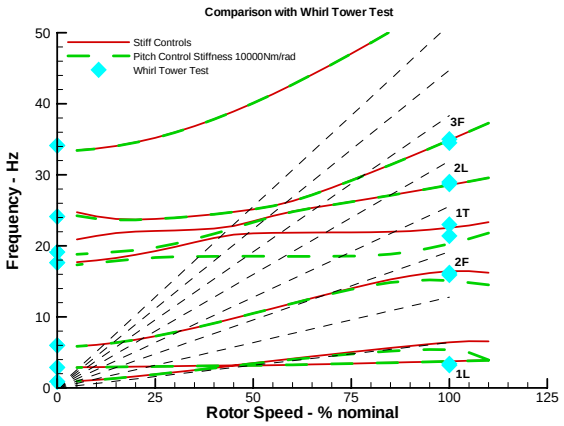

Figure 27: Fan diagram of the ADASYS rotor

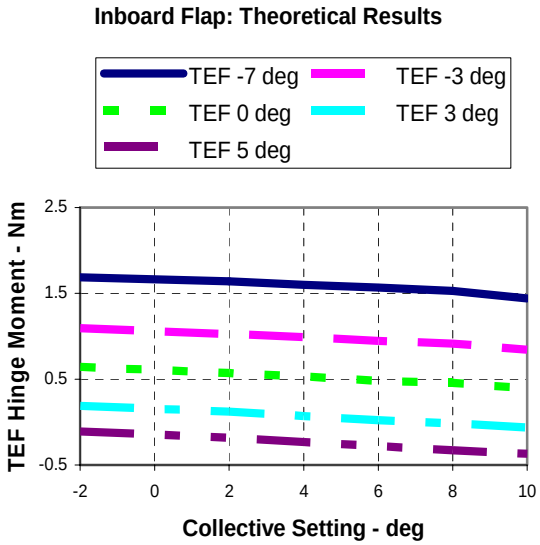

Figure 28: Calculated hinge moments for inboard trailing edge flap

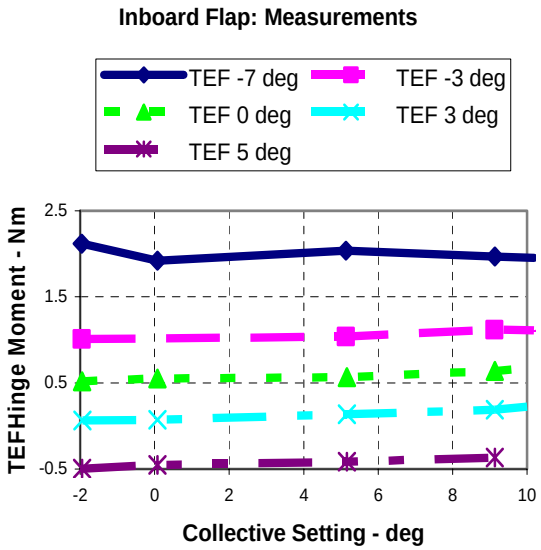

Figure 29: Measured hinge moments for inboard trailing edge flap

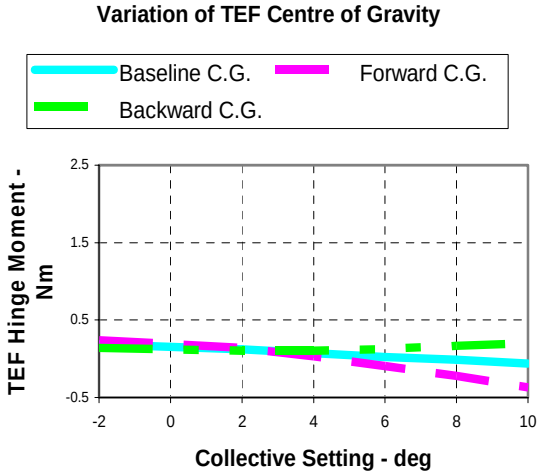

Figure 30: Chordwise variation of trailing edge flap centre of gravity

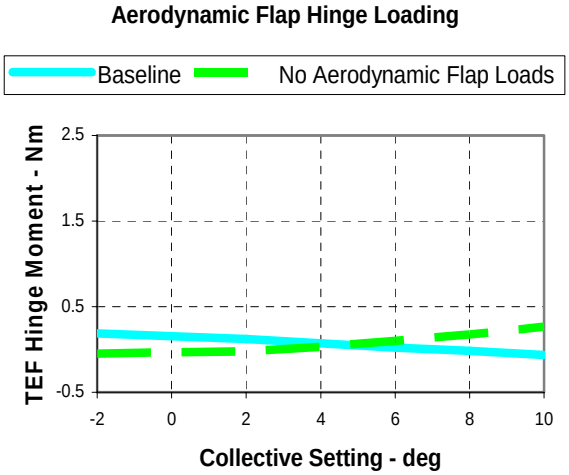

Figure 31: Comparison of hinge moments with and without aerodynamic loading

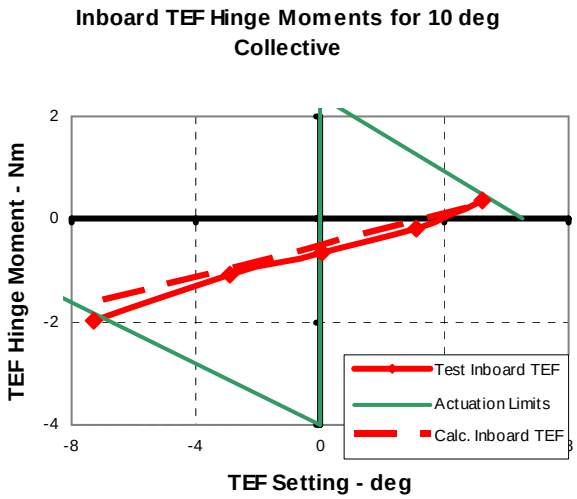

Figure 32: Comparison of inboard TEF hinge moments

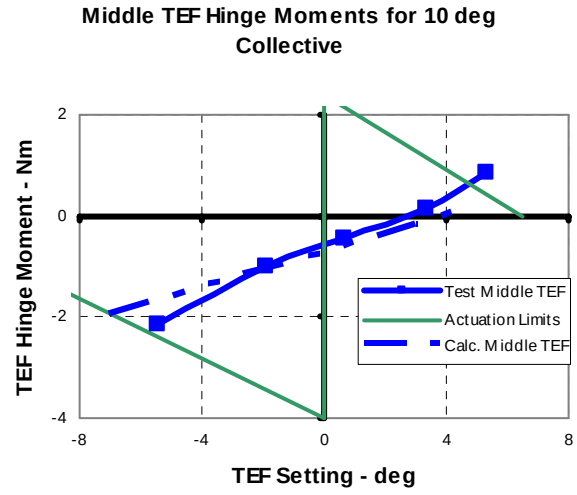

Figure 33: Comparison of middle TEF hinge moments

The control of the trailing edge flaps can be performed in two different modes: Either the commanded flap deflection is mapped onto a corresponding voltage in a feedforward path leading to deviations by actuation flexibilities and air loads or the flap deflection is monitored and adjusted to the prescribed deflection by an inner loop modifying the voltage until the commanded TEF deflection is achieved. The later case was tested in detail on the whirl tower whose major results are presented in figures 34 to 36.

The effect of the low torsion frequency is clearly demonstrated by both experimental and analytical results with different inflow models in figure 34 showing high amplitudes for the low harmonics. High amplitudes for low actuation frequencies are also observed for blade flap moments as presented in figure 35. In this case, the response is dominated by the second blade flap mode. Figure 36 shows the results of blade lag bending. The differences of the lag bending moments at the blade passage frequency might be related to drive train dynamic characteristics of the whirl tower test stand which are not covered by the theoretical model.

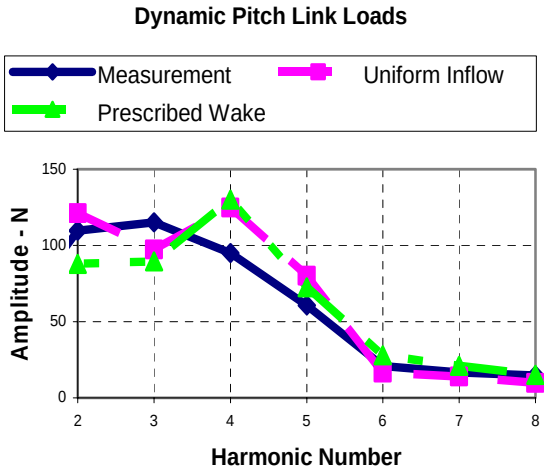

Figure 34: Comparison of dynamic pitch link loads

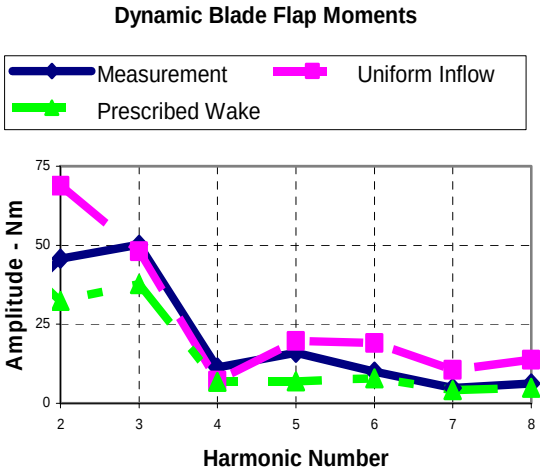

Figure 35: Comparison of blade flap moments

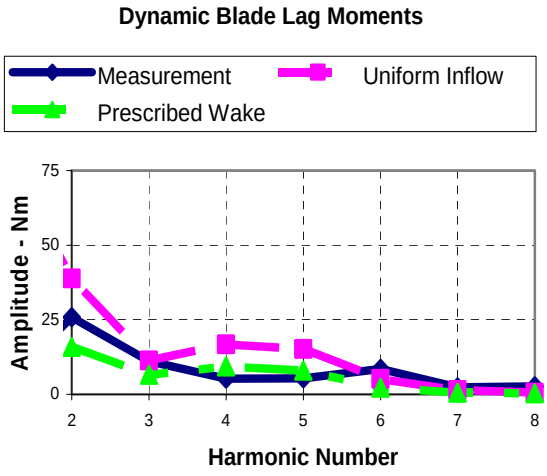

Figure 36: Comparison of blade lag moments

Level Flight: Theoretical and Experimental Results

For the vibration controller design point at 100 KTAS, comprehensive investigations were performed with respect to vibratory hub load controllability at blade passage frequency. The studies also comprised the influence of different inflow models (uniform inflow - UI, rigid wake - PW, free wake - FW) and compared the results with those obtained by a linearized time invariant system (LTI) used for controller design. In order to describe the controllability by target figures, the hub load increments were calculated for 6 deg TEF deflection angle at 12 different phase angles and the amplitudes averaged and normalised to 1 deg for each inflow model. The column plots in the following figures 37 to 39 show the results for the vertical hub force, the hub roll and the hub pitch moment at blade passage frequency for actuation frequencies of 3/rev, 4/rev and 5/rev for the case of the position controller engaged. Generally, the amplitudes are in acceptable agreement; the uniform inflow results predicting the highest results in most cases as already noted above for the axialsymmetric cases.

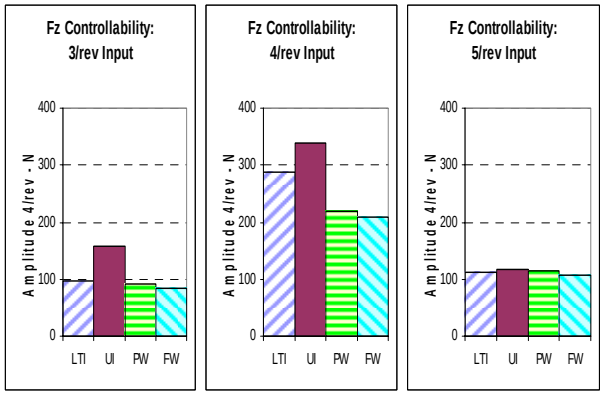

Figure 37: Comparison of 4/rev vertical hub force increments at 100 KTAS due to 1 deg TEF input

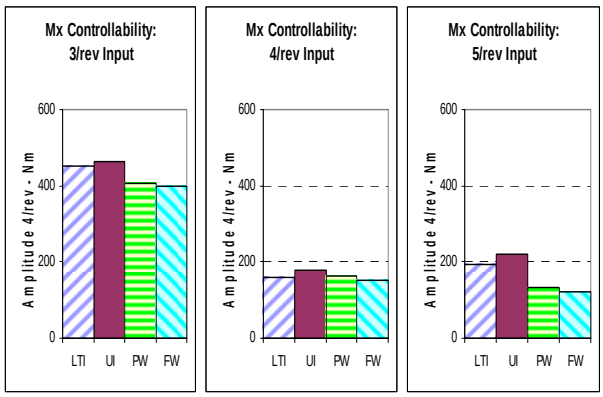

Figure 38: Comparison of 4/rev hub roll moment increments at 100 KTAS due to 1 deg TEF input

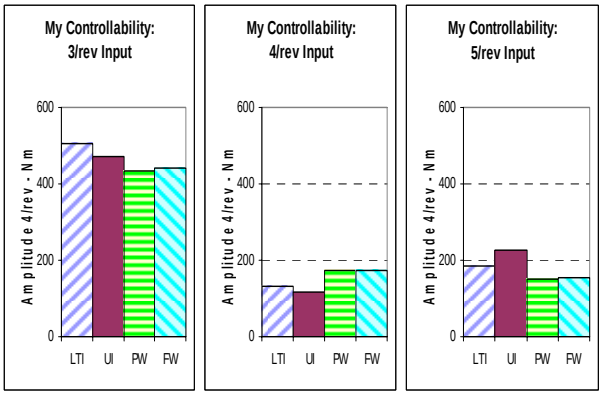

Figure 39: Comparison of 4/rev hub pitch moment increments at 100 KTAS due to 1 deg TEF input

In order to study the behaviour of the rotor system versus flight speed, the linearized system was analysed for different flight speeds with respect to controllability. The following figures 40 to 42 show the controllability of selected vibratory hub loads for the range from 0 to 140 KTAS level flight. The dependency of coupling effects with flight speed is clearly visible; see 3/rev or 5/rev TEF input affecting the vertical hub force at blade passage frequency or 4/rev TEF input affecting vibratory hub roll and pitch moment. A robust vibration controller has to adequately address these characteristics.

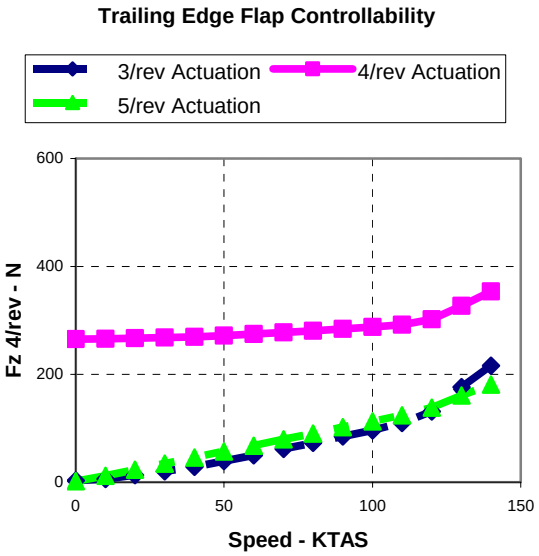

Figure 40: 4/rev vertical hub force increments due to 1 deg TEF input

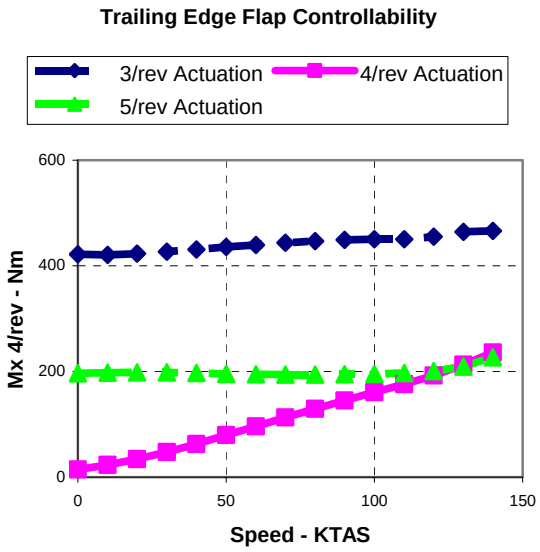

Figure 41: 4/rev hub roll moment increments due to 1 deg TEF input

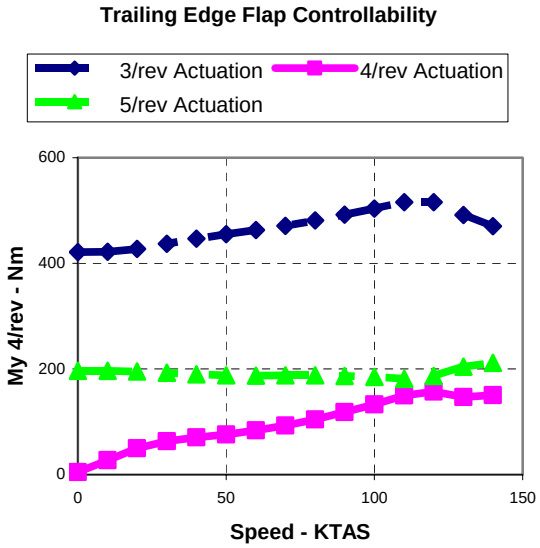

Figure 42: 4/rev hub pitch moment increments due to 1 deg TEF input

In the meantime, first flights with the experimental rotor system were performed aiming on the gathering of vibratory flight test data, figure 43. 4/rev gearbox accelerations are adequate sensor data in order to assess the performance of the active rotor system without taking into account the dynamic properties of the airframe. The following figures 44 to 49 show the controllability of the gearbox vibrations for 60 kts and 100 kts flight speed with a voltage level of 40% compared to the full capacity of the actuators. In this case, the voltage was applied in feedforward mode to the actuators; thus it is not possible to link the trailing edge deflections directly to prescribed flap angle amplitude.

These results confirm the capability of the trailing edge flaps to significantly affect vibrations of the helicopter. Furthermore, it should be noted that the local vibration minima occur for different input phase angles with respect to the two investigated flight speed thus asking for a vibration controller who is able to deal with different flight speeds.

Figure 43: First flight of a helicopter with piezo actuated trailing edge flaps

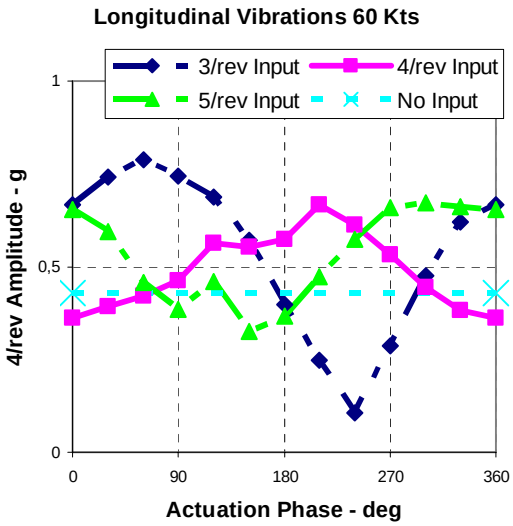

Figure 44: 4/rev longitudinal gear box vibrations with 40% TEF amplitude, 60 kts

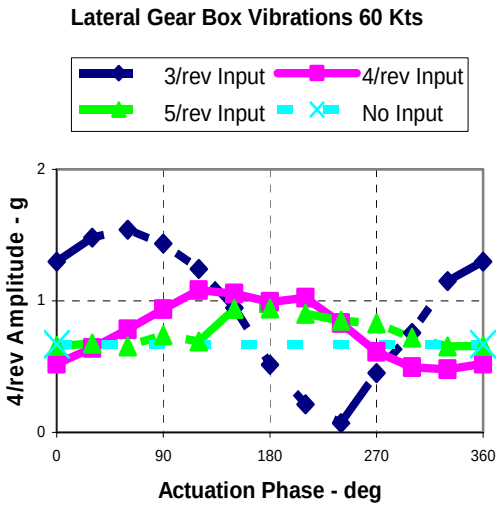

Figure 45: 4/rev lateral gear box vibrations with 40% TEF amplitude, 60 kts

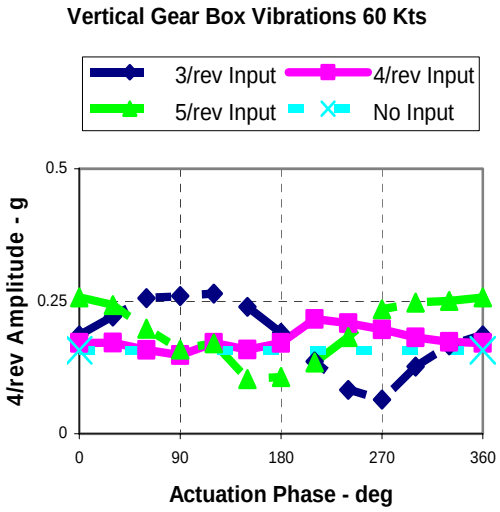

Figure 46: 4/rev vertical gear box vibrations with 40% TEF amplitude, 60 kts

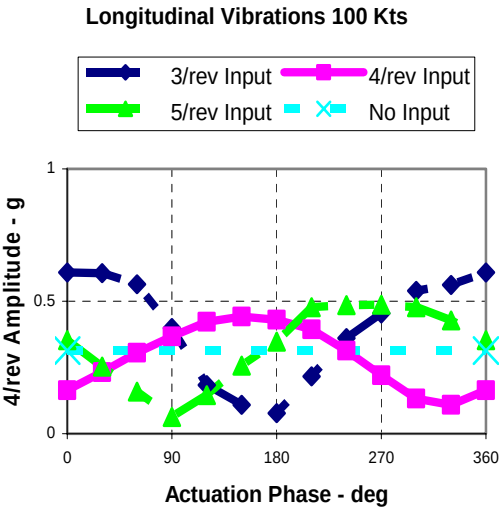

Figure 47: 4/rev longitudinal gear box vibrations with 40% TEF amplitude, 100 kts

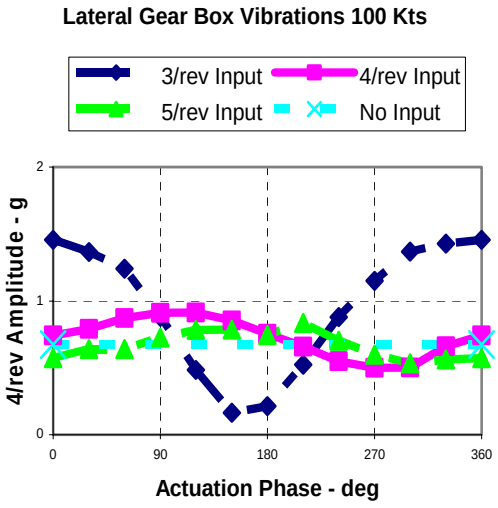

Figure 48: 4/rev lateral gear box vibrations with 40% TEF amplitude, 100 kts

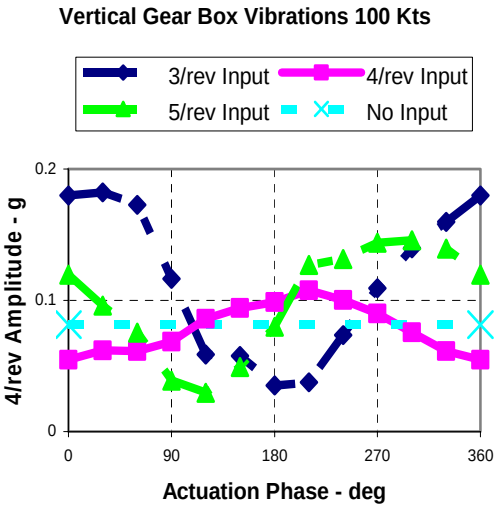

Figure 49: 4/rev verical gear box vibrations with 40% TEF amplitude, 100 kts

Conclusions and Outlook

This paper presents the evolution from the blade root actuated IBC system tested on a BO105 towards a four-bladed active rotor system with trailing edge flaps currently flown on the BK117. The trailing edge flaps are actuated by piezo elements. The main results are summarized as follows:

1. Detailed parameter studies are presented with respect to the optimisation of the trailing edge flap design. Design parameters of interest are flap chord length, flap span and flap position. For vibration control, it is shown that especially the selection of the flap position is very sensitive.

2. Based on these parameter investigations, the realised rotor incorporates a flap chord ratio of 15.6%, a flap span ratio of 10.9% and a flap center position of 74.5%.

Experimental campaigns on the whirl tower test stand confirmed the selected design of the active rotor system.

3. Predictions of vibratory hub load controllability demonstrated an adequate potential of the rotor system for level flight conditions with respect to 3/rev, 4/rev and 5/rev input.

4. This potential was confirmed by flight tests showing a significant reduction of vibrations even for moderate trailing edge flap actuation for 60 kts and 100 kts level flight.

Next, short-term activities will focus on system identification used for the design of the vibration controller and the testing of the vibration controller itself. Furthermore, mid-term steps of the experimental system are under way for an in-flight tracking controller as well as aeromechanical stability improvement by active control. Additional fields suitable for active rotor control are identified with respect to load reduction, stall delay and rotor power improvements. These activities are accompanied by comprehensive studies towards the serialisation of such kind of active systems.

Appendix

The application of thin airfoil theory allows the extension of the existing airfoil tables by entries for non-zero flap angles using the following linearization (1), (2) and (3):

$$c_L(\alpha, M, \eta) = c_L(\alpha, M) + \frac{\partial c_L}{\partial \eta}(M)\eta \qquad (1)$$

$$= c_L(\alpha, M) - \frac{\partial c_L}{\partial \alpha}(M)\frac{\partial \alpha}{\partial \eta}(M)\eta \qquad (2)$$

$$c_M(\alpha, M, \eta) = c_M(\alpha, M) + \frac{\partial c_M}{\partial \eta}(M)\eta \qquad (3)$$

Hereby, the angle of attack for zero lift changes according to (4):

$$\frac{\partial \alpha}{\partial \eta} = -\frac{\partial c_L}{\partial \eta} / \frac{\partial c_L}{\partial \alpha} \qquad (4)$$

Derivativa of lift and moment coefficients are evaluated based on thin airfoil theory, inviscid and incompressible flow according to [14], see (5), (6) and (7):

$$\left(\frac{\partial c_L}{\partial \alpha}\right)_{M=0} = 2\pi \qquad (5)$$

$$\left(\frac{\partial \alpha}{\partial \eta}\right)_{M=0} = -\frac{2}{\pi}\left(\sqrt{\lambda(1-\lambda)} + \arcsin\sqrt{\lambda}\right) \qquad (6)$$

$$\left(\frac{\partial c_M}{\partial \eta}\right)_{M=0} = -2\sqrt{\lambda(1-\lambda)^3} \qquad (7)$$

These derivativa describe an attached flow behaviour thus limiting the applicability of this approach to flap angles of a few degrees around the neutral flap position. Nevertheless, this theoretical restriction poses no real limitation for the studies of the envisaged actuation concept as the realizable flap deflection is constrained to about +/- 10 deg due to hardware restrictions. Concerning compressibility effects, reference [14] suggests to apply the Prandtl-Glauert rule for the subsonic flow regime leading to the following formulas (8) and (9):

$$\frac{\partial c_L}{\partial \eta}(M) = \frac{1}{\sqrt{1-M^2}}\left(\frac{\partial c_L}{\partial \eta}\right)_{M=0} \qquad (8)$$

$$\frac{\partial c_M}{\partial \eta}(M) = \frac{1}{\sqrt{1-M^2}}\left(\frac{\partial c_M}{\partial \eta}\right)_{M=0} \qquad (9)$$

The application of the Prandtl-Glauert rule limits the compressible aerodynamic flap model to a Mach number significantly below unity. If applications occur asking for higher Mach number (e.g. high speed applications for active flaps at outboard stations) the tables will have to be completed by wind tunnel test data or additional CFD results accounting for significant non-linear effects in the transonic region.

As already mentioned the numerical results obtained by the Navies-Stokes formulation were used for calibration of the empirical effectiveness factor κ introduced by [14] in order to account for viscous flow, finite airfoil thickness and other effects not covered by thin airfoil theory.

$$\frac{\partial \alpha}{\partial \eta} = \lambda + \kappa\left[\left(\frac{\partial \alpha}{\partial \eta}\right)_{\kappa=1} - \lambda\right] \qquad (10)$$

$$\frac{\partial c_M}{\partial \eta} = \kappa\left(\frac{\partial c_M}{\partial \eta}\right)_{\kappa=1} \qquad (11)$$

In figures 50 to 55, computational results labelled Navier-Stokes build the reference for the evaluation and calibration of the flap model within the airfoil table files. Three values of the calibration parameter κ ranging from 0.7 to 1.0 are assigned to the flap model in order to allow an appropriate adjustment of the calibration parameter with respect to the CFD results. κ=1 means perfect behaviour of the aerodynamic coefficients regarding the thin airfoil theory.

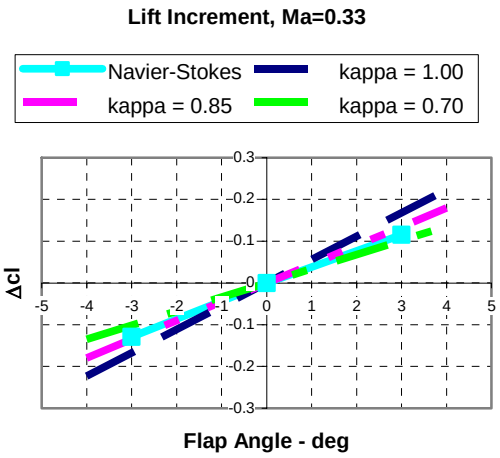

Figure 50: Lift coefficient increment by deflected TEF for low Mach number

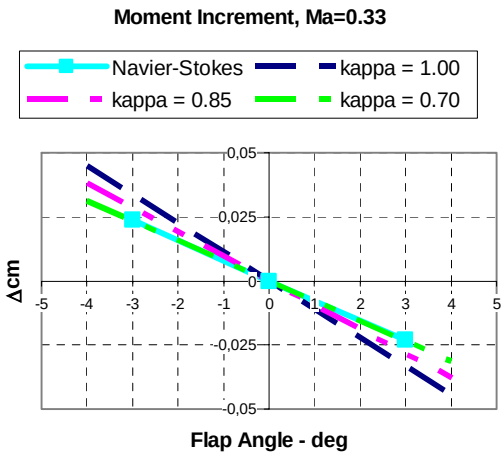

Figure 53: Moment coefficient increment by deflected TEF for low Mach number

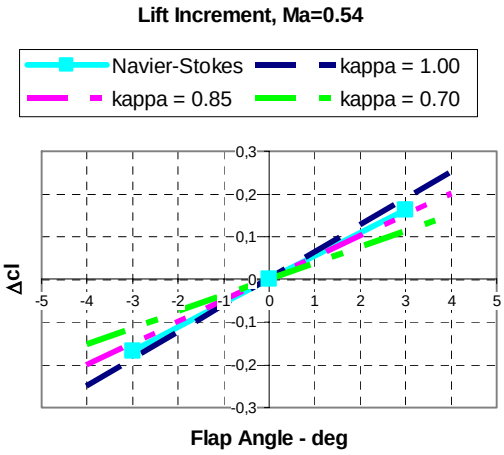

Figure 51: Lift coefficient increment by deflected TEF for intermediate Mach number

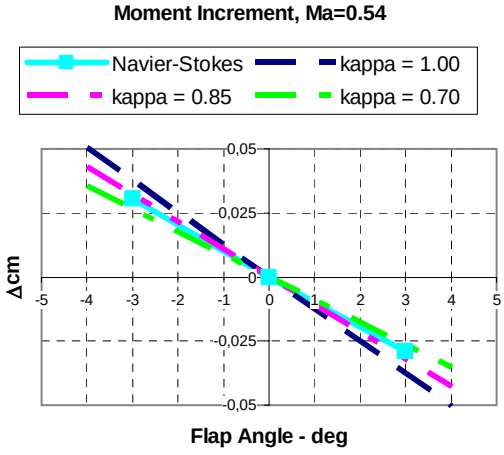

Figure 54: Moment coefficient increment by deflected TEF for intermediate Mach number

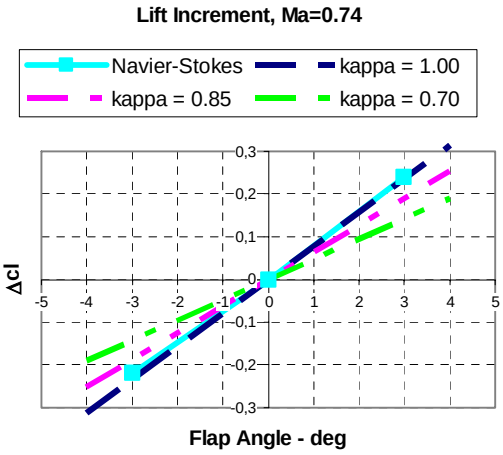

Figure 52: Lift coefficient increment by deflected TEF for high Mach number

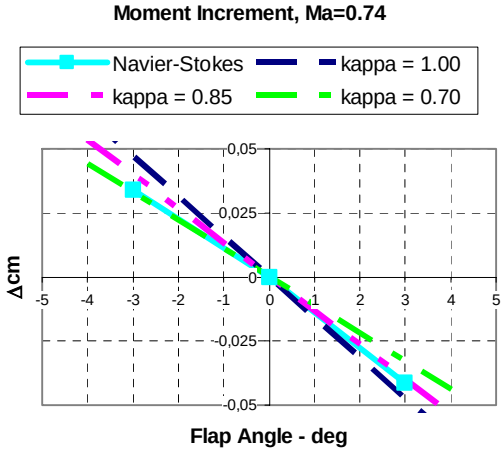

Figure 55: Moment coefficient increment by deflected TEF for high Mach number

In figures 50 to 52, the amount of additional lift coefficient due to flap deflection is shown versus the trailing edge flap angle. The Mach number effect leading to increasing gradients with increasing Mach number are represented by both thin airfoil theory and CFD computations. Nevertheless, the compressibility effect observed by CFD is obviously more significant than by thin airfoil theory as for low Mach numbers $\kappa \approx$ 0.75 to 0.85 and for high Mach numbers $\kappa \approx$ 0.90 to 1.00.

In figures 53 to 55, a similar behaviour is shown for the additional moment coefficients induced by the trailing edge flap. Similar to the lift coefficient increments, Mach number effects of the CFD results are slightly more significant than for thin airfoil theory. Here again, appropriate value of κ are in the range from 0.70 to 0.80 for low Mach numbers and 0.90 to 1.00 for high Mach numbers.

The corresponding behaviour of both moment and lift coefficient leads to the decision to use only one parameter κ for the calculation of the lift and moment coefficient increments caused by the trailing edge flap. For the following studies, the parameter κ is selected to 0.80 which seems to be a fairly good value for the low Mach number region and which is a more conservative choice for the high Mach number region. As the theory behind these formulas is based on inviscid flow, no expression is given for the increase of drag by a deflected flap. Therefore, this aerodynamic flap model is not well suited for investigations concerning rotor torque and rotor power requirements without additional consideration of the flap induced airfoil drag.

The above mentioned aerodynamic coefficients c_L, c_D and c_M are total values related to the ensemble of blade and trailing edge flap. For the analysis of actuation requirements, the airfoil tables were extended by the aerodynamic hinge moments[1]. For the evaluation of flap hinge moments a very approximate approach is used for the aerodynamic load due to limited available data for the baseline airfoil section. The airfoil database lacks of hinge moment data without deflected trailing edge flap. Therefore, an approximation for the relationship $c_{fM} = c_{fM}(\alpha, M)$ was established first. This relationship is related to the pressure distribution in the vicinity of the trailing edge of the airfoil section and depends significantly on the airfoil shape. Afterwards, thin airfoil theory is applied in order to get moment increments for non-zero deflections of the flap.

[1] CAMRAD II offers also the possibility to additionally consider flap lift and flap drag for the calculation of flap hinge forces. This option was not used here and the related coefficients were zeroed.

For incompressible flow, a linear relationship $c_{fM} = c_{fM}(\alpha) = a_1\alpha + a_0$ is assumed to be a good approximation for the investigated operating conditions. Of course, this dependency uses the assumption of small angles of attack for the rotor blade section equipped with the trailing edge flap. For vibration reduction purpose under cruise flight conditions this condition is assumed to be fulfilled.

In order to establish the linear relationship by the information given above in the table, the hinge moment coefficients obtained by CFD are transformed to incompressible flow (M=0) assuming that the Prandtl-Glauert rule is applicable with respect to the aerodynamic flap hinge moment. In figure 56, both compressible and incompressible values of the coefficients are presented for comparison for $\lambda = 0.15$. The compressibility effects for low and medium Mach number are of minor order whereas for high Mach number the difference between compressible and incompressible data is obvious.

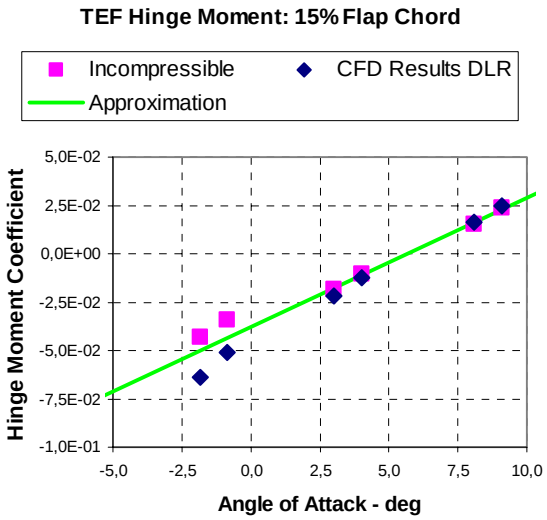

Figure 56: Trailing edge flap hinge moment

The data points for low and medium Mach numbers are estimated to be more appropriate as collocation points for the linear relationship between angle of attack and flap hinge moment coefficient. In figure 56, the straight line represents the modelled behaviour of the flap hinge moment coefficient for incompressible flow. For compressible flow, the Prandtl-Glauert rule is applied to the flap hinge moment coefficient limiting this approach to the subsonic region corresponding to the establishment of the other coefficients, see (12):

$$c_{fM}(\alpha, M) = \frac{a_1\alpha + a_0}{\sqrt{1 - M^2}} \qquad (12)$$

For a deflected trailing edge flap, derivativa are evaluated which are consistent to the theoretical approach used for the derivation of total lift and moment coefficients, see (13), (14) and (15):

$$c_{fM}(\alpha, M, \eta) = c_{fM}(\alpha, M) + \frac{\partial c_{fM}}{\partial \eta}(M)\eta$$

$$= \frac{a_1 \alpha + a_0}{\sqrt{1-M^2}} + \frac{\partial c_{fM}}{\partial \eta}(M)\eta \qquad (13)$$

$$\left(\frac{\partial c_{fM}}{\partial \eta}\right)_{M=0} = -\frac{4\lambda^2}{\pi}\sqrt{\lambda(1-\lambda)}\left[\arcsin\sqrt{\lambda} - \sqrt{\lambda(1-\lambda)}\right] \qquad (14)$$

$$\frac{\partial c_{fM}}{\partial \eta}(M) = \frac{1}{\sqrt{1-M^2}}\left(\frac{\partial c_{fM}}{\partial \eta}\right)_{M=0} \qquad (15)$$

In order to account for compressibility effects, the derivativa are modified using Prandtl-Glauert's rule. As already mentioned, an empirical correction factor κ for lift and moment coefficients was introduced leading to reduced load increments for a given flap angle. In contrast, no corrections of this kind are applied here for flap hinge moments in order to get more conservative values. A comparison between theory and CFD calculations leads to the conclusion that flap hinge moments of the CFD calculations reach a level of about 85% with respect to theoretical values for the investigated trailing edge flap.

Furthermore, the gradient $\partial c_{fM}/\partial c_L$ obtained by the above mentioned linear approximation presented is compared to the corresponding theoretical formula (16)

$$\left(\frac{\partial c_{fM}}{\partial c_L}\right)_{M=0} = -\frac{\lambda^2}{2\pi}\left[(3-2\lambda)\sqrt{\lambda(1-\lambda)} - (3-4\lambda)\arcsin\sqrt{\lambda}\right] \qquad (16)$$

Again, theory overestimates the flap hinge moments. In this case, the gradient derived from CFD calculations amounts approximately 90% of the theoretical value.

Acknowledgements

The authors gratefully acknowledge Dr. Valentin Klöppel of ECD for the administrative support of this challenging project, EADS-CRC for design and provision of the powerful actuation system and Mr. Daniel Glaser for the provision of numerical results.

References

[1] Straub, F., Kennedy, D., "Design, Development, Fabrication and Testing of an Active Flap Rotor System", 61st AHS Annual Forum, Grapevine, Texas, June 2005

[2] Milgram, J, Chopra, I., Straub, F., "A Comprehensive Rotorcraft Aeroelastic Analysis with Trailing Edge Flap Model: Validation with Experimental Data", 52nd AHS Annual Forum, Washington, DC, June 1996

[3] Patt, D., Liu, L., Friedmann, P., „Rotorcraft Vibration Reduction and Noise Prediction Using a Unified Aeroelastic Response Simulation", 59th AHS Annual Forum, Phoenix, Arizona, May 2003

[4] Bebesel, M., Roth, D., Pongratz, R., "Reduction of BVI Noise on Ground – In-flight evaluation of Closed-Loop Controller", 28th European Rotorcraft Forum, Bristol, UK, September 2002

[5] Roth, D., "Advanced Vibration Reduction by IBC Technology", 30th European Rotorcraft Forum, Marseille, France, September 2004

[6] Gläßel, H., Kahl, J., Dieterich, O., Rudolph, S., "Neural Networks for BVI system identification", 29th European Rotorcraft Forum, Friedrichshafen, Germany, September 2003

[7] Dieterich, O., "Application of modern control technology for advanced IBC systems", 24th European Rotorcraft Forum, Marseille, France, 1998

[8] Enenkl, B., Kloeppel, V., Preißler, D., Jänker, P., „Full Scale Rotor with Piezoelectric Actuated Blade Flaps", 28th European Rotorcraft Forum, Bristol, United Kingdom, September 2002

[9] Bebesel, M., Schoell, E., Polz, G., „Aerodynamic and Aeroacoustic Layout of ATR (Advanced Technology Rotor)", 55th AHS Annual Forum, Montreal, Canada, May 1999

[10] Johnson, W., "Technology drivers in the development of CAMRAD II", AHS Aeromechanics Specialists Conference, San Francicso, California, 1994

[11] Schimke, D., Jänker, P., Wendt, V., Junker, B., „Wind Tunnel Evaluation of a Full Scale Piezoelectric Flap Control Unit", 24th European Rotorcraft Forum, Marseille, September 1997

[12] Geissler, W., Sobieczky, H., Vollmers, H., „Numerical Study of the Unsteady Flow on a Pitching Airfoil with Oscillating Flap", 24th European Rotorcraft Forum, Marseille, France, 1998

[13] Hasegawa, Y., Katayama, N., Kobiki, N., Nakasato, E., Yamakawa, E., Okawa, H., „Experimental and Analytical Results of Whirl Tower Test of ATIC Full Scale Rotor System", 57th AHS Annual Forum, Washington, DC; May 2001

[14] Schlichting H., Truckenbrodt E., Aerodynamik des Flugzeuges, Volume 2, Springer-Verlag Berlin Heidelberg New York, 1969, pp.434 - 448